Permeability of three-dimensional fracture networks

N. Koudina, R. Gonzalez Garcia, and J.-F. Thovert
LCD-PTM, CNRS, SP2MI, Boulevard 3, Teleport 2, 86960 Futuroscope Cedex, France

P. M. Adler
IPG, Tour 24, 4 place Jussieu, 75252 Paris Cedex 05, France

(Received 13 August 1997; revised manuscript received 1 December 1997)

The permeability of a three-dimensional network of polygonal fractures is determined by triangulating the network and solving the two-dimensional Darcy equation in each fracture. The general triangulation methodology and the numerical solution are presented. Networks of regular hexagonal fractures are detailed; finite-size scaling is used to analyze the data relative to the percolation threshold, but the conduction exponent t is found close to its classical value in three dimensions; for large fracture densities, permeability is shown to tend towards the mean-field model of Snow [Water Resour. Res. **5**, 1273 (1969)]. Finally, the influence of the shape of the fracture is studied and can be rationalized by means of the excluded volume. [S1063-651X(98)07504-7]

PACS number(s): 47.55.Mh, 05.40.+j, 47.11.+j

I. INTRODUCTION

During the past decade, underground waste repository projects and exploitation of hot, dry, rock geothermal energy have spurred studies in fracture networks transport properties. Many site-specific studies have flourished around various projects (see, e.g., [1]), which are generally based on a careful characterization of the structure of the fractured rock mass, with the classical difficulty of deducing three-dimensional information from one- or two-dimensional field data (e.g., [2]). Then the hydraulic properties are computed by using reconstructed model networks, based on the experimental geometrical characteristics, and various flow models. The applications of these site-specific models were restricted to particular situations, mimicking realistic but specific network structures and boundary conditions. Apparently, they were not applied to a systematic parametric study of the influence of the various structural characteristics on the large-scale hydraulic properties.

The major purpose of the present paper is to develop a full solution of the steady flow problem in a general three-dimensional network made of two-dimensional polygonal fractures as illustrated in Fig. 1. A literature survey shows that in most cases, the description is two dimensional [3] or that the three-dimensional network is replaced by a capillary model. The intersection of two fractures is schematized by a channel that joins their centers with an effective hydraulic conductivity that results from simple geometric arguments; this model is improved [1,4,5] by introducing flow channels in the fractures, which results in complex capillary networks. Nordqvist *et al.* [6] went one step further by building the network from a library of fractures with spatially variable apertures for which flow was solved beforehand. However, again, the final representation is a tube model. These capillary models suffer two main flaws. First, the assignment of the bond conductivities is somewhat arbitrary and the assumption that the fluid flows from center to center is unrealistic. Second, only pair intersections are taken into account. To the best of our knowledge, the only truly three-dimensional flow model is due to Andersson and Dverstorp [7]. The flow is solved in each fracture via a boundary element method, while accounting for all its intersections. However, it is again a case-specific study, with adjusted geometrical parameters to match observed data, and the number of fractures in a sample is very limited.

The only attempts to relate geometric and hydraulic properties by general parametric laws were conducted in the framework of percolation theory. Berkowitz and Balberg [8] reviewed the critical behavior near the percolation threshold. Hestir and Long [9] showed that connectivity is a relevant parameter, as already noticed by Rouleau and Gale [3], and successfully modified its definition to obtain a predictive equation for the large-scale permeability of random plane networks of linear fractures. The computer-controlled two-dimensional experiments of Balberg *et al.* [10] are an interesting alternative approach.

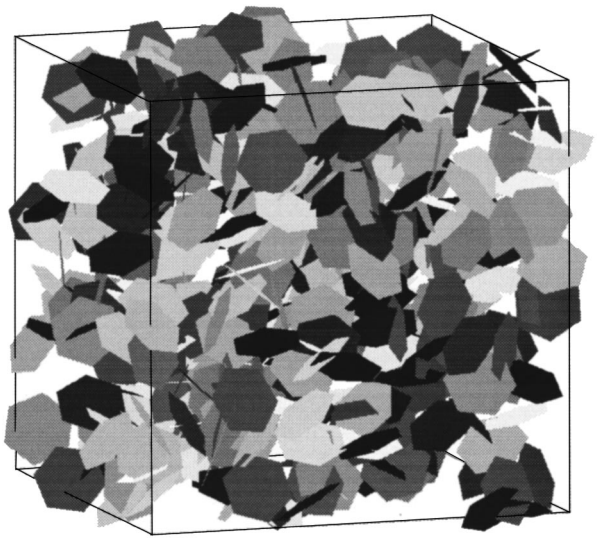

FIG. 1. Example of a three-dimensional fracture network made of identical polygons. The volume of size L^3 contains 495 hexagons; $L=12R$, where R is the radius of the circle in which the hexagon is inscribed.

Our numerical approach involves three main steps, namely, the generation of random fracture networks, the meshing of the network by triangulation, and the solution of the local flow equations with computation of the macroscopic flow properties. The generation procedure and some geometric characterization tools derive from the numerical code of Huseby, Thovert, and Adler [11]. The network triangulation is by far the most difficult task due to the random character of the fracture geometries and of their intersections. Once it is completed, the flow equations are easily obtained by a finite-volume formulation and solved.

This paper is organized as follows. Section II is devoted to the geometrical aspects. The network generation, with prescribed statistical and geometrical parameters such as density of fractures, size, and shape of the fractures, is presented first. The fractures are plane polygons, inscribed in a circle. The triangulation procedure is an advancing front technique [12], which is applied independently to all the fractures, after a few preliminary operations; it is able to operate on any polygonal fracture shape.

Section III is devoted to the flow problem. The flow is ruled by the stationary Reynolds equation at the fracture scale; it is discretized on the triangular mesh by means of a finite-volume formulation and solved under prescribed macroscopic pressure gradients. The global permeability of the fracture network is obtained by integration of the local flow field. Due to the stochastic nature of the generated networks, the generation and solution steps are repeated for a large set of random realizations.

The results are presented and discussed in Sec. IV. As this is a systematic study on this topic, its numerical applications were restricted to networks that are supposed to be statistically homogeneous at a scale much larger than the typical fracture dimension and modeled as spatially periodic, with the fracture locations distributed according to a Poisson law. An illustrative example is treated first and three-dimensional graphical visualizations of the network geometry and flow map are presented. The statistical distribution of the local velocities is determined in a few samples with various densities. Then a wide range of fracture densities is scanned, for a particular fracture shape and varying cell sizes, in order to identify the various regimes and characterize the size effects. The vicinity of the percolation threshold is considered specifically. For moderate or large densities, it is shown that the same kind of power-law holds, with a lower exponent. A linear increase of the permeability with density is reached only for very large densities.

We end the paper with some concluding remarks in Sec. V. Since the numerical tools could handle equally well any orientation distribution, fractures with spatially varying apertures, moderate size distributions, and even specific nonperiodic boundary conditions if needed for a particular case study, various extensions including the interesting case of fractal structures are presented in Sec. V.

II. FRACTURE NETWORKS: GENERATION, CHARACTERIZATION, AND TRIANGULATION

A. Geometry of the fracture network

The fracture networks considered in this work are made of plane polygonal fractures. This assumption is the only requirement to apply the generation, characterization, and triangulation procedures described below and eventually to solve the transport equations. Individual fracture shapes, sizes, or permeabilities and positional or orientational distributions are arbitrary. However, in order to limit this immense field of investigation, we restrict ourselves in this paper to a specific class of fracture networks, which is described now.

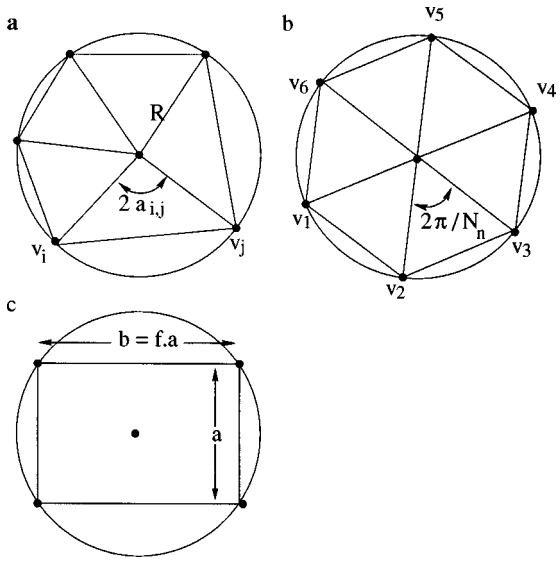

FIG. 2. (a) Definition of the geometry of a polygon inscribed in a circle. Regular polygons such as (b) hexagons and (c) rectangles can be created using appropriate fixed values of the angles.

The network generator has been detailed by Huseby, Thovert, and Adler [11]. Plane polygonal fractures are inserted in a cell τ_0 of size L.

Unless otherwise stated, the following properties hold throughout this paper. The fracture normal vectors are randomly and isotropically distributed and their centers obey a Poisson distribution. The contour of a fracture is a convex polygon, inscribed in a circle of radius R (see Fig. 2). Its N_ν vertices are evenly (for regular polygons) or randomly distributed on this circle. The polygon orientation within its plane is random with uniform distribution. N_ν and R are identical for all the fractures in the network and R is taken as the length unit.

Within this framework, a network is entirely characterized by a fracture shape (N_ν, regular or random), the normalized cell size L/R, and the number of fractures per unit volume. This last quantity can be modified by using the excluded volume V_{ex} introduced by Balberg *et al.* [13]; V_{ex} is defined as the surrounding volume into which the center of another object may not enter if overlap is to be avoided. For example, in a monodisperse population of spheres, V_{ex} is obviously 8 times the sphere volume. For nonspherical objects, the influence of the orientation has to be taken into account in the determination of V_{ex}.

Hence ρ' can be defined as the number of objects per volume V_{ex}; note that in [13] and subsequent papers, the notation V_{ex} refers to the total excluded volume denoted ρ' here and in [11]. In addition, from the definition of V_{ex}, ρ' is also equal to the average number B of intersections per object. ρ' proved very successful in gathering the results for

various geometrical quantities in the class of fracture networks considered here [11].

Analytical expressions of V_{ex} are available only for a few simple shapes. Since for randomly oriented monodisperse disks with radius R in a three-dimensional space, $V_{ex}=\pi^2R^3$ is the half product of the disk area and perimeter [14] and V_{ex} was modeled for polygons in [11] as

$$V_{ex}=\tfrac{1}{2}A_pP_p, \tag{1}$$

where A_p and P_p are the polygon area and perimeter. This model yields a good unified description in terms of ρ' and indeed Eq. (1) is an exact result for a wide class of objects that includes most of the fracture shapes considered here, namely, randomly oriented polygons inscribed in a circle and containing its center.

In addition to the network generator, several geometrical characterization tools from the software developed by Huseby, Thovert, and Adler [11] are applied prior to the triangulation described in the following subsection. First, the fracture intersections are determined. The intersection lines are characterized by their end-point coordinates. Triple points (intersections of three fractures) are also detected. In the applications, there is an important particular case where the network is statistically homogeneous at some macroscopic scale much larger than the typical fracture dimension; in such cases, it is customary to apply periodic boundary conditions to the cell τ_0 of size L; the whole network results from the periodic juxtaposition in space of infinitely many replicas of τ_0. A detailed description of spatially periodic media is given by Adler [15]. In such a case, the percolation of the fracture network is checked along the x, y, and z axes. This is done using a pseudodiffusion algorithm [16]. Since the network is periodic, percolation occurs when two homologous fractures in two different unit cells are connected together. Individual connected components in the network are identified and fractures isolated from the percolating cluster, if any, are labeled and ignored in the solution of the flow problem.

B. Triangulation

In order to solve the flow problem, the fracture network has to be discretized. Since the fractures have polygonal shapes, possibly random, and intersect randomly, the most natural discretization is an unstructured triangulation. This triangulation must obey a few *a priori* constraints: All the original polygon vertices, intersection end points, and triple points (intersections of intersection lines) must coincide with vertices of the triangular mesh; all the original polygon borderlines and fracture intersections must coincide with triangle edges; and the triangulations of two intersecting fractures must match along their intersection line. Except for the last requirement, since the network is a collection of two-dimensional objects, all the fractures may be triangulated independently by any standard two-dimensional algorithm once its initial contour definition has been supplemented with a description of its intersections with other fractures.

A comprehensive review of the existing triangulation methods can be found in [12]. The technique that can comply with the previous limitations the most easily seems to be the advancing front technique, whose application to the present situation is now briefly summarized.

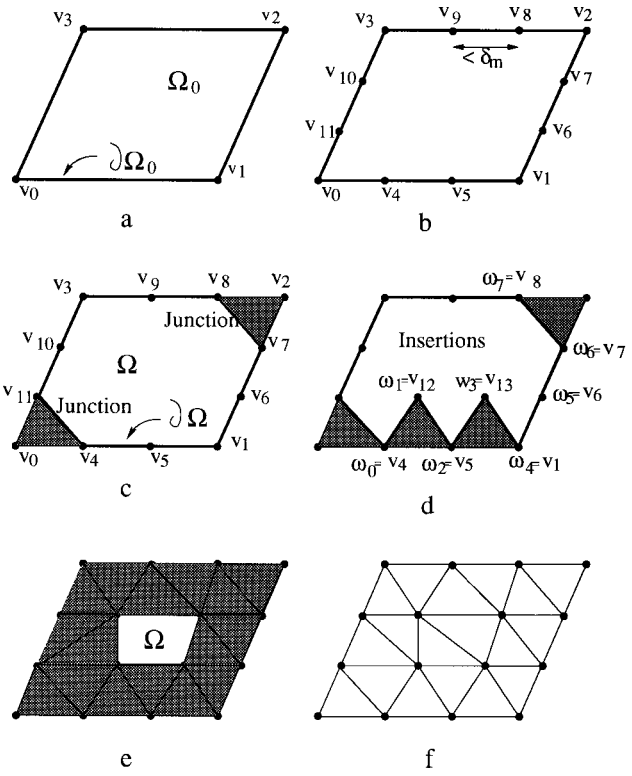

FIG. 3. Typical steps of the triangulation of simple domains by an advancing front method: (a) initial domain Ω_0 with $N_\nu=4$ initial vertices, (b) splitting into segments shorter than δ_M with the $N_0=12$ points of V_0, basic operations of (c) and (e) junction and (d) and (e) insertion, and (f) final stage. The heavy line is the front $\partial\Omega$. The domain Ω still to be triangulated is white, while the part $\Omega_0-\Omega$ of the domain already triangulated is shaded.

As illustrated in Fig. 3, consider the very simple case of a plane convex polygonal contour, which corresponds to an isolated fracture (i.e., a fracture without any intersection with any other fracture). The initial domain is called Ω_0 and Ω is the part of Ω_0 not yet triangulated ($\Omega\subset\Omega_0$ and $\Omega=\Omega_0$ initially). Their contours are $\partial\Omega_0$ and $\partial\Omega$, respectively [Fig. 3(a)]. $\partial\Omega$ is the advancing front. The two basic operations are the junction of two second-neighbor points of the front [Figs. 3(c) and 3(e)], if the resulting triangle is acceptable, and the insertion of a new point within Ω, which constitutes a new triangle when connected with the two facing points of $\partial\Omega$ [Fig. 3(d)]. During these operations, the front $\partial\Omega$ is updated by removal or insertion of points. As can be seen in Fig. 3, $\partial\Omega$ shrinks progressively. The process stops when $\partial\Omega$ reduces to an acceptable triangle.

Now consider the general case where the fracture contains many additional features due to its intersections with other fractures, as displayed in Fig. 4(a). An intersection line may cross the contour only once or twice, thus splitting the fracture into two disjoint domains. It may also lie entirely within the fracture, without any connection with the contour. Several intersection lines, themselves intersecting one another, may enclose internal subdomains with or without connections with the outer contour.

It would of course be possible to handle these subdomains as independent polygonal plane regions and to subsequently assemble their triangulations. Another way was chosen

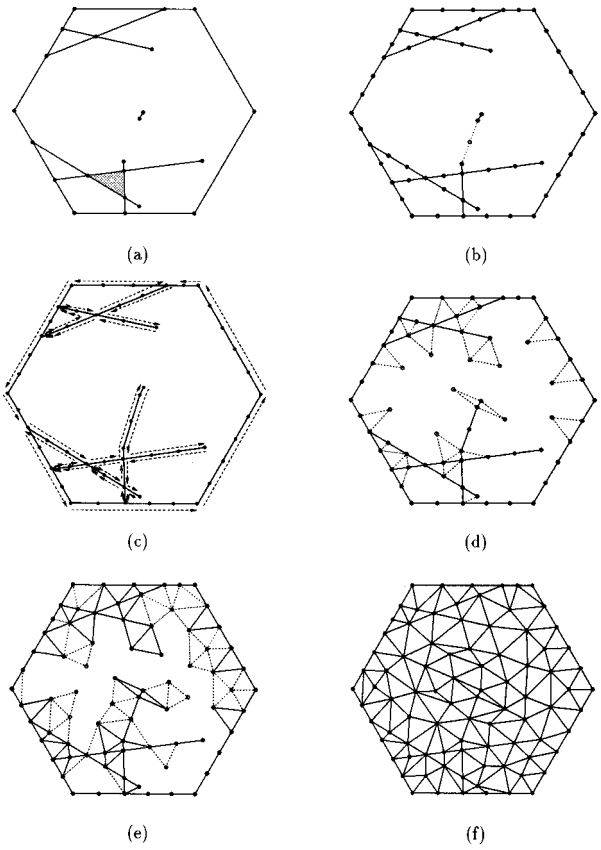

FIG. 4. Successive steps of the triangulation of a complex fracture: (a) initial geometry, which may include intersections lines and inner subdomains (shaded); (b) splitting of the edges into segments shorter than δ_M and connection of all internal features; (c) initial front $\partial\Omega_0$ (the arrows correspond to the spanning cycle). (d) and (e) intermediate and (f) final stages of the triangulation.

here, which allows us to triangulate the whole fracture at once. First, all the internal features are connected to the outer boundary of the fracture [Fig. 4(b)]; all these elements are also split into smaller segments with length smaller than a given value δ_M. Then a cycle $\partial\Omega_0$ that describes the fracture boundary and all its internal features is constructed and treated as the outer contour of a single simply connected (nonconvex) polygon [Fig. 4(c)].

The first set of points to which the advancing front technique is applied consists of the splitted cycle $\partial\Omega_0$. Two remarks are necessary. First, the same rule (with the same δ_M) is applied in all the fractures of the network; a unique splitting is applied to the intersection line of two fractures. Second, during the insertion operation, which consists of throwing a new point v_{Np+1} from a segment (ω_i,ω_{i+1}) of $\partial\Omega$ to create a new triangle [Fig. 3(d)], v_{Np+1} is set so that

$$||\omega_i v_{Np+1}||=||\omega_{i+1} v_{Np+1}||=\delta_I. \tag{2}$$

Initially, δ_I is equal to δ_M, but this value is modified as the process goes. Additional conditions are imposed on this inserted point, e.g., the edges (ω_i,v_{Np+1}) and (ω_{i+1},v_{Np+1}) must not cross any existing edge; for sake of clarity, these conditions are not detailed here. Two intermediate stages and the final result for the example of Fig. 4 are displayed in Figs. 4(d)–4(f).

The procedure above yields for each fracture a collection of triangles, defined by their three vertices. The triangulation of the whole network is the union of all these collections. Recall that the triangulation of intersecting fractures match along their intersection line since the same rule was applied to split it in its two embedding planes. The nodes of the global triangulation are also the union of the points defined in each fracture.

Each triangle belongs to a single fracture, although its edges may belong to two fractures and its vertices to one, two, or three. Note that the fractures that do not belong to a percolating connected component are not triangulated [11]. Thus all the triangles in the list may play a role in the flow, at least for one direction of the pressure gradient.

Whenever necessary, the periodicity of the fracture network (see Sec. II A) is taken into account. Hence the position of each triangle relative to the boundary $\partial\tau_0$ of the unit cell τ_0 needs to be determined. A set of nine integers $j_{n\alpha}$ ($n=1,2,3$ and $\alpha=x,y,z$) is associated with each triangle. If vertex n of a triangle is within τ_0, then $j_n=j_{ny}=j_{nz}=0$. If it is not beyond the cell boundary in the direction of increasing (decreasing) x, then $j_{nx}=+1$ (-1), and similarly for the directions y and z.

To summarize, the output of the triangulation procedure is made of two unstructured lists, which are the list of nodes, defined by their three-dimensional coordinates, and the list of triangles, defined by their vertices, together with the jump conditions mentioned above. In addition, a value of the fracture permeability σ (see Sec. III A) is associated with each triangle.

III. FLOW PROBLEM

A. General equations

The solid matrix containing the fractures is assumed to be impervious. The flow of a Newtonian fluid at low Reynolds number is governed by the Stokes equations within a fracture, i.e., at a local scale characterized by a typical aperture b_0. Because of the classical Poiseuille law, the typical permeability σ_0' of a fracture is expected to be of the order of

$$\sigma_0'=\frac{b_0^3}{12}. \tag{3}$$

Moreover, b_0 is assumed to be much smaller than the typical lateral extent $2R_0=D_0$ of the fracture

$$b_0 \ll D_0. \tag{4}$$

In contrast to [17], the flow is described at a scale $\mathcal{L}$ that is intermediate between b_0 and D_0,

$$b_0 \ll \mathcal{L} \ll D_0. \tag{5}$$

At this scale, the flow is governed by the Darcy equation

$$\boldsymbol{q}'=-\frac{1}{\mu}\boldsymbol{\sigma}\cdot\overline{\boldsymbol{\nabla}' p}. \tag{6}$$

$\boldsymbol{q}$ and $\overline{\nabla' p}$ are the locally averaged flow rate per unit width $[L^2T^{-1}]$ and pressure gradient, and $\boldsymbol{\sigma}[L^3]$ is the fracture permeability tensor. The mass conservation equation becomes

$$\boldsymbol{\nabla}'_S \cdot \boldsymbol{q}' = 0, \tag{7}$$

where $\boldsymbol{\nabla}'_S$ is the two-dimensional gradient operator in the mean fracture plane; it is defined by [18]

$$\boldsymbol{\nabla}'_S = (\boldsymbol{I} - \boldsymbol{nn}) \cdot \boldsymbol{\nabla}', \tag{8}$$

where $\boldsymbol{n}$ is the outer unit normal to the fracture plane and $\boldsymbol{I}$ is the unit tensor. The dependence of $\boldsymbol{\sigma}'$ upon the fracture characteristics was investigated by Mourzenko, Thovert, and Adler [17].

Any standard boundary condition can be applied to this network. For instance, pressures or fluxes could be applied along some inlet and outlet lines $\mathcal{L}_i$ and $\mathcal{L}_o$ drawn on some fractures of the network, for instance

$$p = p_i \quad \text{along} \quad \mathcal{L}_i,$$
$$p = p_o \quad \text{along} \quad \mathcal{L}_o. \tag{9}$$

In the particular case where the fracture networks are statistically homogeneous at the field scale L, which is assumed to be large with respect to the lateral dimensions D_0 of the fractures, $L \gg D_0$, the infinite medium can be represented by the periodic juxtaposition of identical unit cells τ_0 in the three directions of space. When a macroscopic pressure gradient $\overline{\overline{\nabla' p}}$ is applied upon this unbounded medium, the fluid flow is described by Eqs. (6) and (7), together with periodicity conditions for $\boldsymbol{v}'$, $\boldsymbol{q}'$, and $\nabla' p'$ and

$$\overline{\overline{\nabla' p}} = \frac{1}{\tau_0} \int_{\partial \tau_0} p' \, d\boldsymbol{s}'. \tag{10}$$

The seepage velocity $\bar{\boldsymbol{v}}'$ can be evaluated as

$$\bar{\boldsymbol{v}}' = \frac{1}{\tau_0} \int_{\tau_f} \boldsymbol{v}' \, d\tau' = \frac{1}{\tau_0} \int_{S_f} \boldsymbol{q}' \, ds', \tag{11}$$

where τ_f is the interstitial volume of the fractures and S_f their projection on their mean planes. This flux is related to the pressure gradient by Darcy's law [15]

$$\bar{\boldsymbol{v}}' = -\frac{1}{\mu} \boldsymbol{K}' \cdot \overline{\overline{\nabla' p}}. \tag{12}$$

$\boldsymbol{K}'$ is the permeability tensor $[L^2]$, to be determined from Eqs. (11) and (12) once the problem (6) and (7) has been solved. Alternatively, Eqs. (6) and (7) can be solved with a prescribed velocity $\bar{\boldsymbol{v}}'$. The $\overline{\overline{\nabla' p}}$ is evaluated by Eq. (10) and $\boldsymbol{v}'$ is deduced from Eq. (12).

In this paper $\boldsymbol{\sigma}'$ is taken to be uniform over each fracture and identical for all fractures. Permeability variations within the fractures will be addressed in future works. Since all the networks considered here are isotropic, $\boldsymbol{K}'$ is a spherical tensor

$$\boldsymbol{K}' = K' \boldsymbol{I}. \tag{13}$$

B. Dimensionless formulation

The hydraulic aperture b (or a typical value b_0 if all the fractures are not identical) is a characteristic length scale for the fracture aperture. On the other hand, R is the typical fracture extent. These two length scales, together with a reference pressure p_0, can be used to recast the equations in a dimensionless form. Define

$$\sigma_0 = \frac{b_0^3}{12}, \quad q_0 = \frac{\sigma_0 p_0}{\boldsymbol{\mu} R}, \quad U_0 = \frac{\sigma_0 p_0}{\mu R^2}, \quad K_0 = \frac{\sigma_0}{R}. \tag{14}$$

The dimensionless parameters (without primes) are defined by

$$p' = p_0 p, \quad \nabla' = \frac{1}{R} \nabla,$$
$$\boldsymbol{v}' = U_0 \boldsymbol{v}', \quad \boldsymbol{q}' = q_0 \boldsymbol{q}, \tag{15}$$
$$\boldsymbol{\sigma}' = \sigma_0 \boldsymbol{\sigma}, \quad \boldsymbol{K}' = K_0 \boldsymbol{K}.$$

All the following developments use this dimensionless formulation. For isotropic networks, $\boldsymbol{K}$ is a spherical tensor, $\boldsymbol{K} = K\boldsymbol{I}$, and our results will be presented in terms of the dimensionless permeability K.

C. Discretization of the transport equation and numerical implementation

The value of the pressure p must be determined at each of the N_v points m of the triangular mesh. The N_v unknown pressures are determined from N_v equations, i.e., one equation per mesh point, obtained from a flux balance condition, via a second-order finite volume scheme.

The dimensionless Reynolds equation is integrated over nonoverlapping domains Ω_m that surround the mesh point m, as illustrated in Fig. 5. If m belongs to the intersection of two fractures, or even if it is a triple point (intersection of three fractures), Ω_m is simply the union of the two or three domains obtained as above in each fracture [Fig. 5(c)].

In this second-order formulation, both $\boldsymbol{\sigma}$ and ∇p are considered piecewise constant on each triangle. In addition, $\boldsymbol{\sigma}$ is assumed to be isotropic.

Of course, the driving force in these equations is the macroscopic pressure gradient $\overline{\nabla p}$. This quantity occurs when a triangle crosses the boundary $\partial \tau_0$ of the unit cell; the pressures at two neighboring nodes that do not belong to the same unit cell have to be corrected by the pressure drop across the unit cell [15].

Finally, the discretized transport equation can be expressed as the linear system

$$\boldsymbol{A} \cdot \boldsymbol{p} - \boldsymbol{B} = \boldsymbol{0}, \tag{16}$$

where $\boldsymbol{B}$ corresponds to the macroscopic pressure drop. It is easily shown that the matrix $\boldsymbol{A}$ is symmetric. Equation (16) is solved iteratively by a conjugate gradient algorithm. An integral convergence criterion is used:

$$||\boldsymbol{A} \cdot \boldsymbol{p} - \boldsymbol{B}|| \leqslant \eta ||\boldsymbol{B}||, \tag{17}$$

where $||\ ||$ denotes the standard Cartesian norm.

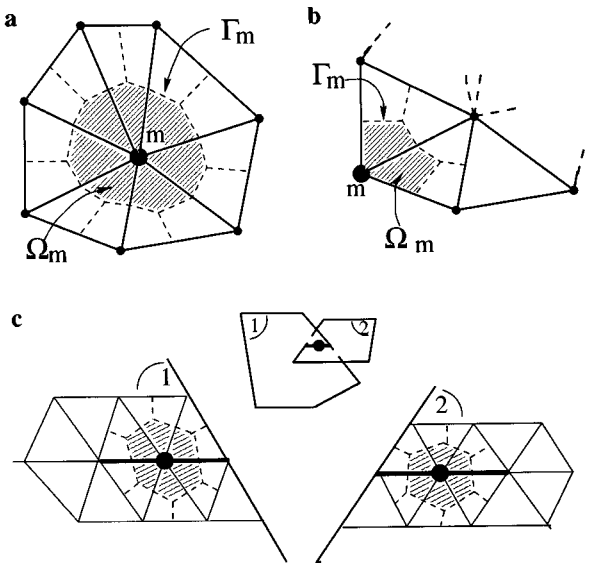

FIG. 5. Finite volume Ω_m surrounding a point m (a) neither on a fracture boundary nor on an intersection, (b) on a fracture boundary, and (c) on a fracture intersection. In (c) the two fractures have been separated for clarity.

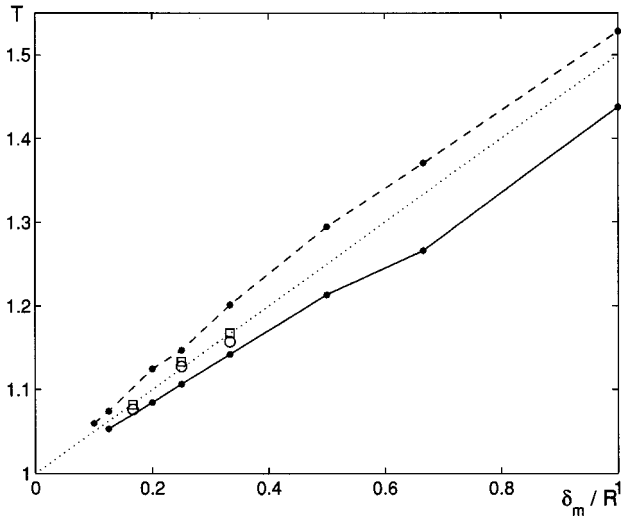

FIG. 6. Normalized trace T of the mean permeability tensor of random networks of regular hexagons as a function of δ_M/R, with $L/R=4$ and $\rho'=2.5$ (broken line) or 4 (solid line). The dotted line is Eq. (19). The symbols □ (○) refer to networks of rectangular fractures, with aspect ratios $f=4$ (6), density $\rho'=4$ (3), and containing 219 (434) fractures.

D. Validation and accuracy of the numerical scheme

Only two nonphysical parameters were introduced in the numerical scheme, namely, the mesh coarseness δ_M and the convergence criterion η. Their influence on the computed permeability should vanish as each of them tends toward 0.

A few simple tests were successfully passed by the numerical code, such as the insensitivity to a shift of the unit-cell boundaries or a permutation of the axes of coordinates. Then the numerical results were compared to a few analytical solutions. Unfortunately, situations where exact solutions can be obtained are very limited. Networks where the percolating component reduces into strips of constant width, made of one or several fractures intersecting at arbitrary angles, can be worked out, with or without simple permeability variations inside the fractures. The relative departures of the numerical permeabilities from the theoretical predictions did not exceed 0.6% or 1.5%, with $\delta_M/R=\frac{1}{4}$.

A more complex configuration is made of four families of parallel plane channels, with their intersections on a face-centered-cubic lattice. The unit cell, of size L^3, contains four mesh points and 32 triangles. The numerical calculations yield the exact analytical solution [see Eq. (31) and the related comments]

$$\boldsymbol{K}'=\frac{8}{\sqrt{3}L}\sigma\boldsymbol{I}. \tag{18}$$

While these tests show that the numerical scheme is basically correct, such simple situations cannot be used to quantify the influence of the mesh coarseness. Therefore, another series of tests was conducted with random networks of regular hexagonal fractures. Several samples were built with $L/R=4$ and $\rho'=2.5$ or 4. These two densities are representative of near-critical and well-connected networks, respectively.

The typical mesh size δ_M was varied from R to $R/10$. In all cases, all the components of the permeability tensor decrease as the resolution is improved. The variations are fairly linear when plotted against δ_M/R, as done in Fig. 6, for the average trace T of $\boldsymbol{K}$. In this plot, the values of K are normalized by the linear extrapolation K^∞ when δ_M vanishes. As a rule of thumb, a permeability tensor component K_{ij}^∞ can be deduced from the computed result K_{ij} for finite δ_M/R by

$$K_{ij}=K_{ij}^\infty\left(1+\frac{\delta_M}{2R}\right). \tag{19}$$

In all the cases considered here, the application of Eq. (19) to all the results for $\delta_M\leqslant R/2$ yields the corresponding K_{ij}^∞ within $\pm 3\%$.

It is apparent from Eq. (19) that a 5% accuracy requires $\delta_M/R\approx 0.1$. Unfortunately, such a resolution is unaffordable in many applications, in terms of both computation time and memory requirement. Typical values for a small case (64 regular hexagons with $\rho'=4$ and $L/R=4$) are given in Table I for various coarsenesses. The computation time was measured on a powerful IBM RISC station. These values refer only to the triangulation step. It should be noted that the

TABLE I. Typical number of triangles $N_{\rm tr}$, computation time T in minutes, and memory requirement M in megabytes for the triangulation of a network containing 64 regular hexagons with $\rho'=4$ and $L/R=4$ for various coarsenesses δ_M/R.

δ_M/R	$N_{\rm tr}$	T	M
$\frac{2}{3}$	1900	$\frac{1}{2}$	5
$\frac{1}{3}$	2700	1	6
$\frac{1}{2}$	5000	4	11
$\frac{1}{4}$	8200	10	18
$\frac{1}{5}$	12 000	30	30
$\frac{1}{8}$	28 000	230	110

solution of the flow problem is less demanding since the required memory is less and the computation time is about five times shorter.

Clearly, the requirements for $\delta_M/R=1/8$ are very demanding. It was also felt that tripling the time and doubling the memory was not worth the gain in accuracy from 12% to 10% as expected from Eq. (19). Therefore, unless otherwise stated, all the data given in this paper were obtained with $\Delta_M/R=\frac{1}{4}$. Most of the systematic 12–15 % systematic error would be compensated by applying Eq. (19). Furthermore, since Eq. (19) applies fairly well for various fracture shapes and densities, our discussions relative to the exponents in the limit cases or the comparison of various fracture shapes are unaffected by the mesh coarseness effects.

Two additional remarks can be made before closing this discussion. On the one hand, the triangulation step could be significantly speeded up by use of a hierarchical algorithm. A coarse triangular mesh could be built first and then refined until the desired mesh density is reached instead of building directly a fine mesh by using the advancing front method. On the other hand, the key to an accurate solution of the flow problem does not necessarily lie in a very fine but uniform mesh. Great improvements can be expected instead by conditional local refinements of an otherwise coarse mesh, according to criteria derived from the flow field. These two features will be implemented in the near future.

Note also that in its current implementation, the triangulation procedure fails for very dense networks, without any influence of the sample size. With $L/R=4$, 100% of the samples are successfully triangulated for $\rho'\leqslant 6$ and 90% for $\rho'=10$. For larger densities, the success rates drops dramatically from 40% for $\rho'=12$ and down to 0.5% for $\rho'=16$. In the latter case, it is almost certain (probability $\geqslant 99\%$) that at least one fracture in the network intersects at least 24 other ones. This unfortunately restricts the range of densities that can be addressed. These limitations should be removed in the near future.

IV. RESULTS

Three main subjects are addressed in this section. First, a very simple illustrative example is presented. Second, some velocity histograms are discussed. Third, the influence of density of the permeability of networks of monodisperse regular hexagons is analyzed. Finally, in order to check the relevance of the normalized density ρ' to characterize the hydraulic properties of a fracture network, a wide variety of polygon shapes are investigated for two constant densities.

A. Illustrative example

Prior to systematic data, a complete graphical illustration of a very simple case is given here. In order to obtain readable pictures, a small sample of six fractures was taken, with $L/R=3$. The unit cell is displayed in Figs. 7(a) and 7(b) with various viewing angles. In Fig. 7(c) four unit cells are displayed in order to make the percolating path more visible. The fractures in Fig. 7 are triangulated with $\delta_M/R=\frac{1}{2}$. The connections between the fractures are sketched in Fig. 7(d).

The fracture network was triangulated and the flow field was computed for $\delta_M/R=\frac{1}{2}$, $\frac{1}{3}$, $\frac{1}{4}$, $\frac{1}{5}$, and $\frac{1}{8}$. Figures 8(a)–8(e) display the results relative to the various values of δ_M/R for fracture 4. The flow features in Fig. 8(f) are very clear. The fluid enters the fracture from fractures 2 and 3 on the left and leaves it towards fractures 5 and 1 on the right. Some areas are nearly stagnant, while in others most of the total flux is concentrated. The flux field is discontinuous across the intersection lines. All the features in Fig. 8(f) are visible in Figs. 8(a)–8(e) with less resolution. The total fluxes across the network computed for increasing resolution, normalized by the value for $\delta_M/R=\frac{1}{8}$, are 1.113, 1.051, 1.033, 1.018, and 1. Note that fracture 4, like fracture 1 but unlike 2, 3, 5, and 6, is critical for percolation. Therefore, the whole flux through the network crosses the critical midsection of fracture 4 in Fig. 8. The triangulation size $\delta_M/R=\frac{1}{4}$ used in all subsequent computations corresponds to Fig. 8(c).

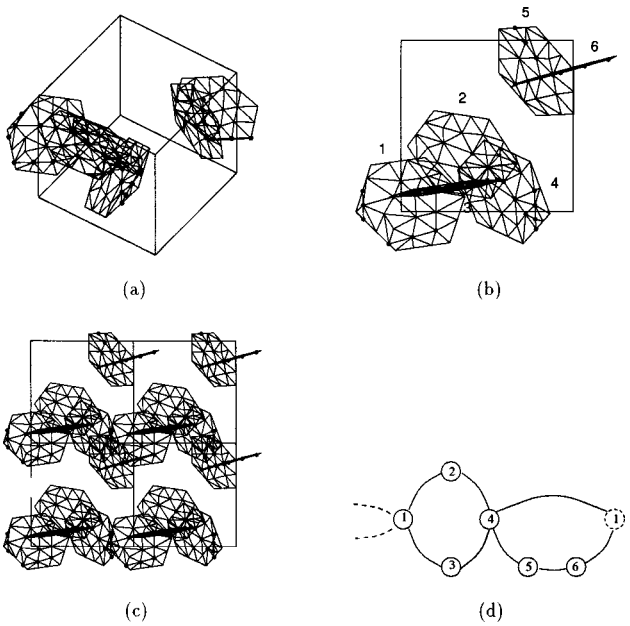

FIG. 7. Example of network of six equisized regular hexagonal fractures with $L/R=3$: (a) and (b) unit cell from two different viewing angles, (c) four neighboring unit cells, and (d) sketch of the fracture connections. The fractures are triangulated with $\delta_M=R/2$.

B. Local velocity distribution

The visualizations in the preceding paragraph show that intense flow and quasistagnant zones coexist in the fractures that belong to the percolating component. This feature is of crucial importance for the dispersion of a convected species, such as heat or a Brownian solute. It can be illustrated further by use of the histograms of the local fluid velocities. Six networks were considered, with various densities ranging from $\rho'=\rho_c'$ to 8. Their characteristics are summarized in Table II. They contain 128–320 fractures. The triangulation was performed with $\delta_M/R=\frac{1}{4}$, which yielded 18 000–33 000 triangles. For the lower densities, many fractures are not connected to a percolating cluster; only 1.5% remain isolated for $\rho'=4$ and the network is totally connected for $\rho'\geqslant 6$.

Figure 9 displays the histograms of the local flow rate q in the triangles (left column) or averaged over the fractures (right column), normalized by the normal $q^*=\overline{v}/\mathcal{S}$ of the average of $\boldsymbol{q}$ over all the fractures. $\mathcal{S}$ is the volumetric fracture surface area $\mathcal{S}=S_f/\tau_0$. Note that the histograms aver-

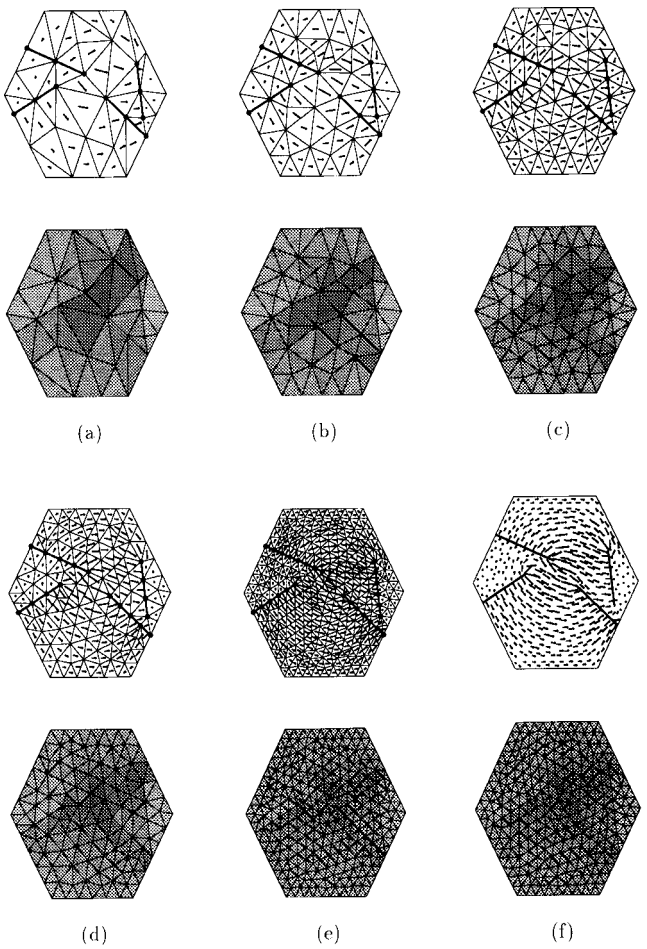

FIG. 8. Fracture 4 in the network of Fig. 7 for various triangulations $\delta_M/R=\frac{1}{2}$ (a), $\frac{1}{3}$ (b), $\frac{1}{4}$ (c), $\frac{1}{5}$ (d), and $\frac{1}{8}$ (e) and (f). In each upper picture, the triangulation is displayed and black dots are mesh points common with another fracture. The arrow lengths are proportional to the local flux density. In the lower pictures, the gray levels are proportional to the flux intensity, normalized by its maximum value within the fracture. (f) is similar to (e), but the triangulation is not displayed. The heavy lines are the intersection with other fractures.

aged over the fractures are more noisy because of the relatively small number of fractures.

The apparently bimodal distribution for the lower densities is an artifact due to the global convergence criterion (17). All these computations were run with $\eta=10^{-5}$. For low densities, many fractures that are connected to the percolating component are actually dead ends and carry no flow; hence a small erratic random number is obtained in the numerical resolution. This was confirmed by solving the flow problem in the network with $\rho'=2.3$ with a finer convergence criterion $\eta=10^{-7}$; as expected, the peak for the lower flow rates is shifted by two orders of magnitude [Fig. 9(a)].

TABLE II. Characteristics of the networks in Fig. 9: density ρ', sample size L/R, number of fractures in the network $N_{\rm fr}$ and in the percolating component $N_{{\rm fr},c}$, and number of triangles in the connected fractures $N_{\rm tr}$.

Fig. 9	ρ'	L/R	$N_{\rm fr}$	$N_{{\rm fr},c}$	$N_{\rm tr}$
(a)	2.3	10	295	118	14 842
(b)	2.5	10	320	209	26 549
(c)	3	8	197	168	21 408
(d)	4	8	262	258	33 342
(e)	6	6	196	166	22 267
(f)	8	5	128	128	18 372

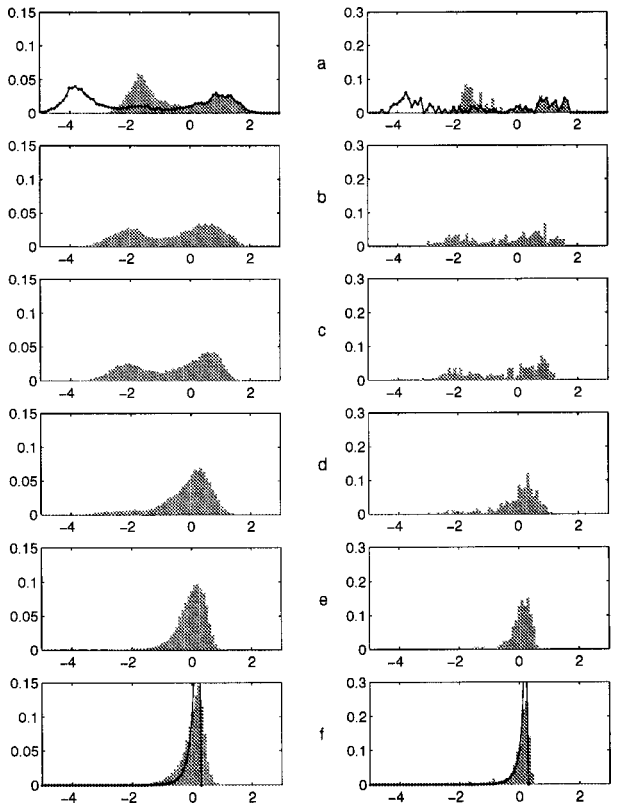

FIG. 9. Histograms of the normalized flow rate q/q^* in the triangles (left) or averaged in the fractures (right), in the networks of Table II with the same convention $a,b,\ldots,f$ (gray bars). The abscissas are decimal logarithms. $\delta_M/R=\frac{1}{4}$ and $\eta=10^{-5}$. The curves in (a) were obtained with $\eta=10^{-7}$. The curves in (f) are the distribution (20).

Thus the leftmost peak should be ignored and a unimodal distribution, though asymmetric with a very long tail, is obtained in all cases. As the density ρ' grows, the quiescent zones disappear and the histogram tail shortens accordingly. Simultaneously, new flow paths are opened to the flow and the highest velocities, which correspond to flow amplifications in a few critical areas, disappear also. The velocity distribution becomes narrower and the peak more acute, though it never becomes log-normal; instead, it seems to be very close to the distribution

$$f\left(\frac{q}{q^*}\right)=\frac{2}{3}\,\frac{\dfrac{2q}{3q^*}}{\sqrt{1-(2q/3q^*)^2}},\quad 0\leqslant\frac{q}{q^*}\leqslant\frac{3}{2},\qquad(20)$$

as expected in Snow's [19] model, made of infinite randomly oriented plane channels (see Sec. IV C).

All these comments hold for both sets of histograms for the local velocities in the triangles or for the average velocities in the fractures. However, the convergence towards Eq.

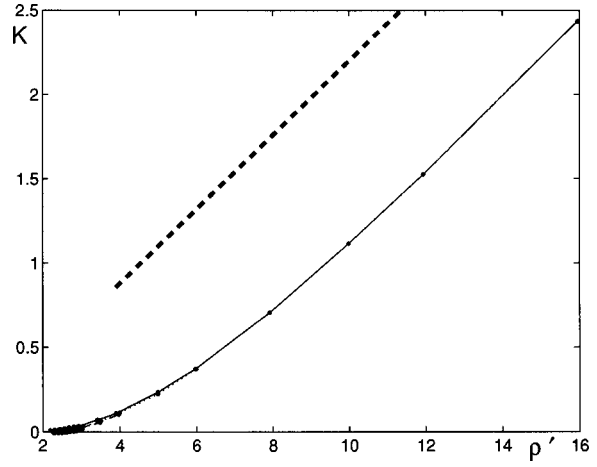

FIG. 10. Dimensionless permeability K of networks of monodisperse regular hexagonal fractures as a function of the density ρ' (Cartesian plot). Data are for $L/R=4$ (——●——), 5 (···●···), 6 (– – –●– – –), 8 (–·–●–·–), and 10 (——○——). The heavy broken line is Eq. (34).

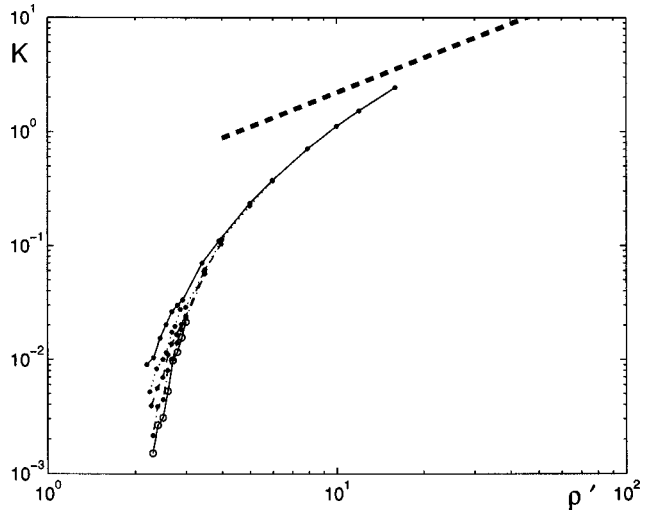

FIG. 11. Dimensionless permeability K of networks of monodisperse regular hexagonal fractures as a function of the density ρ' (log-log plot). Data are for $L/R=4$ (——●——), 5 (···●···), 6 (– – –●– – –), 8 (–·–●–·–), and 10 (——○——). The heavy broken line is Eq. (34).

(20) is more visible for the averages over the fractures (right column in Fig. 9) because the largest and lowest local values of q are filtered out by the averaging.

C. Influence of the fracture density for monodisperse hexagons

Let us recall first the results relative to the determination of the percolation threshold by Huseby, Thovert, and Adler [11] for monodisperse polygons. Of course, the critical density ρ_c depends upon the shape of the fractures; however, when the excluded volume V_{ex} is used, the critical threshold ρ_c', which is the critical number of fractures per excluded volume, was shown to be a constant equal to 2.22–2.30 for a wide range of polygons.

The permeability of networks of regular monodisperse hexagonal fractures was systematically investigated for cell sizes ranging from $L=4R$ to $10R$ and for normalized densities ranging from slightly below the percolation threshold $\rho_c'=2.3$ up to $\rho'=12$. The specific value $\rho_c'=2.3$ obtained for regular hexagons is used here.

All the data for $\rho'\leqslant 2.4$ are statistical averages over 400 random realizations. All the results for $\rho'>2.4$ are averages over 100 samples. The average permeability K in the following plots is defined as one-third of the trace of the average permeability tensor, which is always close to isotropy as expected since no anisotropy is introduced in the stochastic network construction procedure.

The whole data set is displayed in various representations in Figs. 10, 11, and 14. Figure 10 provides a Cartesian plot of the average permeability K against the density ρ', which provides a general view of the variations. Two zones are clearly visible on this plot; close to the percolation threshold, K tends towards zero, with an influence of the size of the unit cell, as discussed below. At large density, the variations of K are a linear function of ρ'. It will be seen that there might be a third region that does not show up in this representation; this intermediate region ranges from $\rho'\sim 3$ up to $\rho'\sim 12$. These distinctions will be used to split the discussion of the results into three parts as density increases.

1. Permeability exponent at the percolation threshold

Let us start with the analysis of this interesting region, which is seen better in Fig. 11. Close to the percolation threshold, the conductivity Σ of a site or bond lattice is known to vanish according to a power law [20]:

$$\Sigma\propto(p-p_c)^t, \tag{21}$$

where p is the site- or bond-occupancy probability and p_c its critical value. The correlation length ξ (mean size of a connected cluster) is also ruled by a power law

$$\xi\propto(p-p_c)^{-\nu}. \tag{22}$$

The exponents t and ν are believed to be universal, i.e., to depend only on the space dimensionality d, but not on the underlying lattice properties. In three dimensions, the following values are generally accepted [20]:

$$\nu=0.88, \quad t=2.0. \tag{23}$$

The percolation theory for lattices can be applied to continuum percolation. It has been established over the past 15 years that the proper equivalent to the probability p is the mean number of intersections per object. Therefore, scaling laws similar to Eqs. (21) and (22) are expected

$$K\propto(\rho'-\rho_c'), \quad \xi\propto(\rho'-\rho_c')^{-\nu}. \tag{24}$$

However, it has been argued (see [21,8,14] and references therein) that in continuum percolation, the exponent t might depend upon the geometrical model. The reason is that in contrast to lattice systems, the conductances of bonds in a continuous network may be determined by the geometry and, indeed, models have been designed where the distribution of bond conductances yields a nonuniversal behavior.

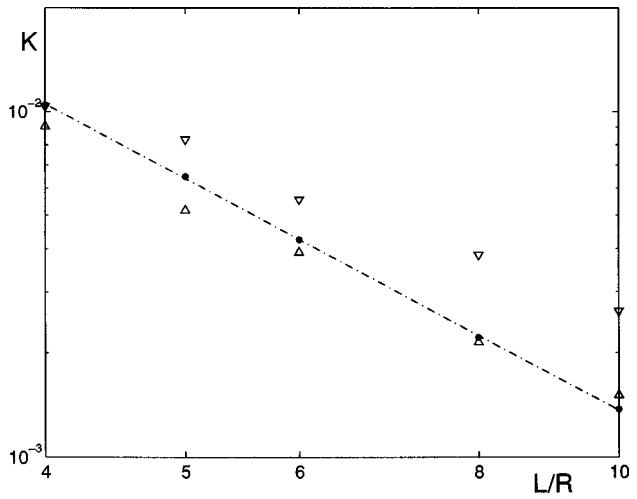

FIG. 12. Dimensionless permeability K at the percolation threshold $\rho_c'=2.3$ in networks of monodisperse regular hexagonal fractures as a function of the sample size L/R (●), deduced by linear interpolation from the permeabilities K^- and K^+ for ρ'^- (△) and ρ'^+ (▽). The dashed line is the least-squares fit (26).

The finite-size scaling technique [22,20] has been applied here to determine the permeability exponent for random networks of regular hexagonal fractures. At the percolation threshold, ξ is larger than any finite cell size and the permeability scales as

$$K(\rho_c',L)\propto L^{-t/\nu}. \tag{25}$$

Because of the divergence of ξ, K depends upon the ratio L/R, close to ρ_c', as it is illustrated by Fig. 11, where significant finite-size effects start occurring at $\rho'\sim 4$.

K was computed for networks at $\rho'=\rho_c'$ for cell sizes ranging from $L=4R$ to $10R$. The permeability was averaged over 400 realizations in each case. The number of fractures in the unit cell ranged from 18 to about 300. Since the number of fractures in a finite cell is necessarily an integer, it was not possible to set exactly ρ' to ρ_c', especially for the smallest cells. For instance, with $L=4R$, 18 and 19 fractures correspond to $\rho'=2.19$ and 2.31, respectively. Therefore, K was computed for two values of ρ' equal to ρ'^- and ρ'^+ below and above ρ_c'; the corresponding values are denoted K^- and K^+; $K(\rho_c',L)$ was estimated from a linear interpolation between these two values.

The results are displayed in Fig. 12. The straight line is the least-squares fit of the interpolated values

$$K(\rho_c',L)=0.23L^{-2.23}, \quad r=0.999\,92. \tag{26}$$

A small digression about the equality of ρ' and the mean number of intersections per fracture has to be made here. If the fractures were truly distributed according to a Poisson law, the total number of intersections N_I and the number of fractures $N_{\rm fr}$ in a large enough domain would verify $2N_I=\rho' N_{\rm fr}$ if ρ' is defined as the number of fractures per excluded volume. However, the representation of the network by the periodic juxtaposition of finite unit cells introduces a cutoff that makes the distribution only approximately Poissonian since the content of a unit cell is prescribed to the expected value for a domain with the same volume instead of being a random variable with the same average. This has some consequences for the number of fracture intersections. For instance, if the unit cell contains a single fracture, no intersection is possible and $N_I=0$; if it contains two fractures, $N_I=V_{\rm ex}/L^3$. More generally, N_I, $N_{\rm fr}$, and ρ' are related by $2N_I=\rho'(N_{\rm fr}-1)$, as illustrated in Fig. 13. This deviation from a true Poisson distribution has little effect when the cell size or the fracture density is large, but when $N_{\rm fr}$ is as low as 20, ρ' and the number of intersections per fracture may differ by a few percent.

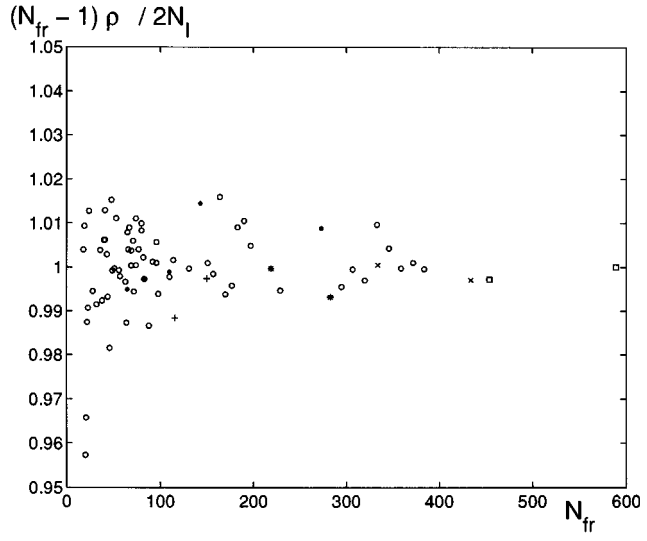

FIG. 13. Ratio $(N_{\rm fr}-1)\rho'/2N_I$ in fractures networks versus the number of fractures $N_{\rm fr}$. Data are for monodisperse regular hexagonal fractures with $L/R=4$, 5, 6, 8, and 10 (○); monodisperse random quadrilaterals, hexagons, and dodecagons with $L/R=4$ or 5 (●); and monodisperse rectangles with aspect ratios $f=2$ (+), 4 (*), 6 (×), and 8 (□).

The fit (26) was obtained by using the actual average value of $2N_I/(N_{\rm fr}-1)$ in the networks for interpolating $K(\rho_c',L)$ between K^- and K^+. If the number of fractures per excluded volume (ρ') is used instead, we get

$$K(\rho_c',L)=0.20\ L^{-2.14}, \quad r=0.998. \tag{27}$$

Finally, if we use the quantity $2N_I/N_{\rm fr}$, we obtain

$$K(\rho_c',L)=0.30\ L^{-2.30}, \quad r=0.9992. \tag{28}$$

The comparison of Eqs. (26)–(28) provides an estimate of the accuracy of the determination of t/ν,

$$t/\nu=2.22\pm 0.08. \tag{29}$$

It is in very good agreement with the universal value $t/\nu\approx 2.3$ in three dimensions from [20]. A universal behavior was also observed in the computer-controlled two-dimensional experiments of Balberg *et al.* [10].

Let us conclude this subsection by recalling that the networks are three-dimensional structures made of special two-dimensional objects that are flat polygons (see Fig. 1). The previous result shows that these networks still belong to the same universality class as standard percolation networks made of sites or bonds [20].

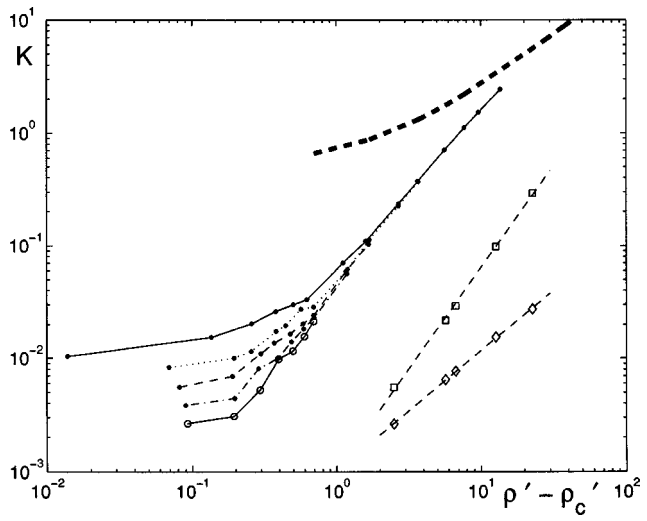

FIG. 14. Dimensionless permeability K of networks of monodisperse regular hexagonal fractures as a function of $\rho' - \rho_c'$ (log-log plot). Data are for $L/R = 4$ (——●——), 5 (···●···), 6 (– – –●– – –), 8 (–·–●–·–), and 10 (——○——). The heavy broken line is Eq. (34) and the symbols ◇ and □ are the original and modified data of Cacas [23], together with the fits (35) and (36), in arbitrary units.

2. Scalings for intermediate and high densities

Because of the classical scaling law (24), a log-log plot of K against $\rho' - \rho_c'$ is displayed in Fig. 14. The finite-size effects are again visible at low densities, but it might be interesting to note that the data for dense networks fall very accurately on a straight line that corresponds to a power law; a least-squares fit of all the data for $\rho' \geqslant 3.5$, with the largest cell sizes available, yields

$$K = 0.0455(\rho' - \rho_c')^{1.57}, \quad r = 0.9994. \tag{30}$$

However, such a fitting is largely empirical and represents some sort of transition from the critical region to the high-density region, which will now be analyzed.

Snow [19] considered networks where all the fractures are infinite plane channels, with an arbitrary orientation distribution. This is equivalent to assuming that the whole surface of all the fractures in the network may contribute to the flow and can be valid only in the limit of very dense networks. If the plane orientation is characterized by its normal vector $\boldsymbol{n}$ and the fracture density per direction by the surface area of fracture per unit volume $\mathcal{S}'(\boldsymbol{n})$, the permeability tensor is given by

$$\boldsymbol{K}'_{\mathrm{Sn}} = \sigma' \int \mathcal{S}'(\boldsymbol{n})(\boldsymbol{I} - \boldsymbol{nn})\, d\boldsymbol{n}. \tag{31}$$

For instance, Eq. (18) is a particular application of Eq. (31) where the vector $\boldsymbol{n}$ takes only four discrete values, with $\mathcal{S}'(\boldsymbol{n}) = \sqrt{3}/L$. For an isotropic network, $\mathcal{S}'(\boldsymbol{n}) = \mathcal{S}'/4\pi$, where $\mathcal{S}'$ is the total volumetric surface area and $\boldsymbol{n}$ is evenly distributed on the unit sphere. Therefore,

$$\boldsymbol{K}_{\mathrm{Sn}}^{\mathrm{iso}\prime} = \frac{2}{3}\sigma' \mathcal{S}' \boldsymbol{I}. \tag{32}$$

In our random networks, $\mathcal{S}'$ is given by

$$\mathcal{S}' = \rho A_p = \frac{\rho' A_p}{V_{\mathrm{ex}}} = \frac{2\rho'}{P_p}. \tag{33}$$

Finally, the dimensionless permeability in Snow's model network with same surface density is

$$K_{\mathrm{Sn}}^{\mathrm{iso}} = \frac{4}{3}\frac{R}{P_p}\rho'. \tag{34}$$

For regular hexagons, $P_p = 6R$ and $K_{\mathrm{Sn}}^{\mathrm{iso}}$ reduces to $2\rho'/9$; this expression is plotted in Figs. 10, 11, and 14 and is indeed a likely asymptote for very large densities. However, it still overestimates K by a factor 2 at $\rho' = 10$. One may guess from Fig. 14 that Eq. (30) should become invalid for $\rho' \approx 20$ since then it would exceed Eq. (34). Unfortunately, such densities could not be investigated because the triangulation becomes exceedingly difficult, but a negative inflection of the curve $K(\rho')$ is visible in Fig. 14 for $\rho' \geqslant 12$.

Hence it seems that the range of validity of Eq. (30), though very large, is a transition zone between the critical power law near the percolation threshold (24) and the linear growth (34) and that maybe Eq. (30) as no substantiation. It is still of interest, however, for practical purposes, in view of its successful fit over the range of the most common fracture densities.

3. Comparison with other data

As mentioned in the Introduction, we could not find in the literature any systematic study of the dependence of K upon

TABLE III. Three types of monodisperse and two types of polydisperse fracture geometries.

Polygon type	Number of fractures $\rho' = 3$, $L/R = 6$	Number of fractures $\rho' = 4$, $L/R = 5$
regular polygons, $N_\nu = 4,5,6,8,12,20$	67–114	51–88
random polygons, $N_\nu = 4,6,12$	84–273	65–211
rectangles, aspect ratio $f = 1,2,4,6,8$	83–589	64–454
regular hexagons, radius $\in [\frac{R}{2}, R]$ or $[\frac{R}{4}, R]$		146–234
random quadrilaterals, $\alpha_{i,i+1} = \pi/2$ and random radii $\|\|Ov_i\|\| \in [\frac{R}{2}, R]$ or $[\frac{R}{4}, R]$		207–350

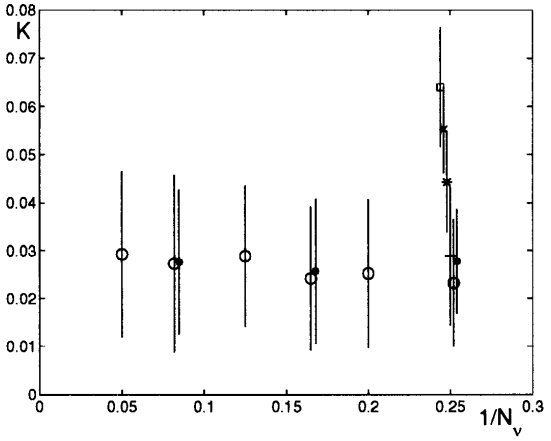

(a)

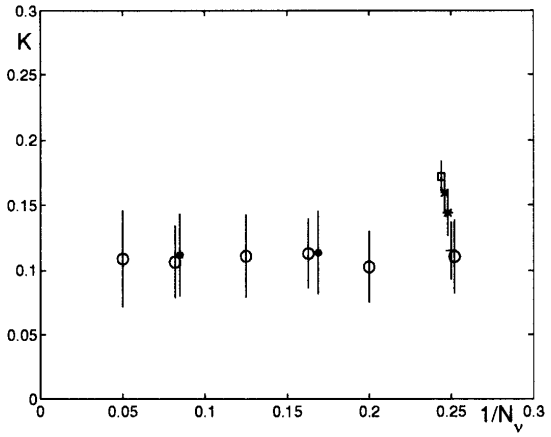

(b)

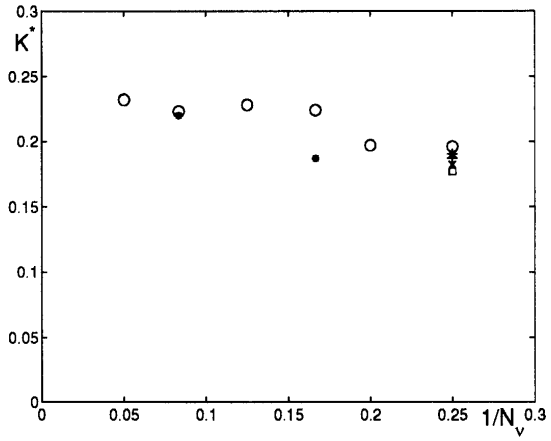

(c)

FIG. 15. Dimensionless permeability (a) and (b)K or (c) K^* in the fracture networks of Table III versus $1/N_v$. In (a), $\rho'=3$ and $L/R=6$ and in (b) and (c), $\rho'=4$ and $L/R=5$. In (a) and (b), some abscissas are slightly shifted to make the statistical error bars visible. Data are for monodisperse regular polygons (○), random polygons (●), and rectangles with aspect ratio $f=2$ (+), 4 (*), 6 (×), and 8 (□).

the fracture density, out of the critical region $\rho' \approx \rho'_c$. The only set of data, due to Cacas [23], was intended to test her numerical code in a simple case before she proceeded with more complex but specific networks, with matched individual fracture permeability distributions.

In this test, Cacas considered random networks of monodispersed and randomly oriented circular fractures. In the flow model, the fracture network was assimilated to a capillary network, with linear bonds joining the centers of intersecting disks. The hydraulic resistances of these bonds were proportional to the center-to-center distance along the fractures, regardless of the width of the intersection line.

The density ρ' (called here n) and the disk radius R were varied simultaneously, with ρ' proportional to R. Five values of ρ' were considered: 4.8, 8, 9, 15, and 25. When normalized according to Eq. (15) the permeability follows very accurately a power law

$$K \propto (\rho' - \rho'_c)^{1.067} \quad (r = 0.9998). \tag{35}$$

It is impossible to relate the prefactor in Eq. (35) with the fracture permeability σ because of the arbitrary definition of the bond conductances. If they are assumed to be functions of the center-to-center distance only, this is equivalent to assuming implicitly that the flow from one fracture to another neighboring one takes place in discrete channels, whose number does not depend on the fracture or intersection linear sizes. Alternatively, one may suppose that the number of channels scales as the disk radius R or even that all the fracture surface contributes to the flow, as in our simulations. With this correction, the data of Cacas [23] follow again a power law of $\rho' - \rho'_c$, but with a different exponent

$$K \propto (\rho' - \rho'_c)^{1.804} \quad (r = 0.9994). \tag{36}$$

It is interesting to note that in both cases the best fitting function is a power law of $\rho' - \rho'_c$. Correlations with a power of ρ' are less successful. Cacas's data and the fits (35) and (36) are plotted in Fig. 14, with an arbitrary prefactor equal to 0.001.

The difference between Eqs. (35) and (36) illustrates the sensitivity of the capillary models on the mean-field arguments used to assign the bond conductivities. The common solution, applied by Cacas [23] and most other authors (see the Introduction), is to assign the bond conductivities randomly, with an *a priori* distribution function (generally lognormal), and to fit its parameters in order to match the results of experimental hydraulic measurements. Recall that if field data relative, e.g., to the fracture aperture (uniform or variable) or permeability distributions are actually available, they can straightforwardly be included in the present simulations.

D. Influence of the fracture shape

The preceding subsection was devoted to a thorough study of a particular fracture shape. Data were obtained over the whole density range and asymptotic laws for low and high densities. We try here to determine whether these results can be applied to any fracture shape, in the general class

described in Sec. II A, if the network is characterized by its density ρ' and a characteristic length scale.

To this end, we consider two particular densities $\rho'=3$ and 4 with cell sizes $L=6R$ and $5R$, respectively. A set of 100 random realizations was generated for each particular case.

Several types of fractures shapes were considered. They are summarized in Table III. The first one consists in regular monodisperse polygons, with $N_\nu=4$, 5, 6, 8, 12, or 20 vertices. The networks in Sec. IV C (regular hexagons) belong to this class, as the limiting case of circular fractures. The second one consists of random polygons with $N_\nu=4$, 6, or 12 vertices, with a constant circumscribed circle radius R. The third class is made of regular monodisperse rectangles, with aspect ratio $f=2$, 4, 6, and 8. The square fractures also belong to this class with $f=1$.

The dimensionless permeabilities K are plotted in Fig. 15 versus $1/N_\nu$, together with the statistical standard deviations. The results for $\rho'=3$ are given in Fig. 15(a). The data for regular polygons are fairly constant; a slight increase is visible as the polygons become more circular ($N_\nu\to\infty$), but these variations are much smaller than the statistical error bars. Furthermore, the permeabilities for the random polygons are quasi-identical to those for the regular ones. On the other hand, the permeabilities of the networks of rectangles are significantly larger than the values for square fractures if $f\geqslant 4$. It was checked (see Fig. 6) that this does not result from the triangulation coarseness, as could have been suspected since δ_M is commensurable with the smaller side of the most slender rectangles.

It is difficult to elaborate much further on these data for networks near the percolation threshold. Although ρ_c' should not depend on the polygon shape and was actually found in the narrow range $2.22\leqslant\rho_c'\leqslant 2.30$ by Huseby, Thovert, and Adler [11] for most polygons in Fig. 15(a) (except for the most anisotropic rectangles, which were not investigated), the finite-size effects could be shape dependent and affect differently the various networks.

The data for $\rho'=4$ in Fig. 15(b) are less sensitive to this artifact. Indeed, the permeabilities for regular and random polygons are all identical within $\pm 5\%$. However, the rectangles still yield much larger permeabilities. It was checked again for the rectangles that the triangulation coarseness is not responsible for the difference (Fig. 6). This discrepancy is probably due to the definition of the characteristic length scale used in Eq. (15) to normalize the permeability. While R is obviously an adequate choice for regular polygons, one may question its relevance for slender rectangles.

Several other length scales may be used instead of R. The most obvious ones are $\langle A_p\rangle^{1/2}$ and $V_{\rm ex}^{1/3}$. The former is suggested by Snow's [19] model [cf. Eq. (31)], whose main parameter is the volumetric fracture surface area, while the latter is introduced naturally in the percolation theory approach. In the present situation, they yield almost identical results. Define the dimensionless permeability K^* by

$$\boldsymbol{K}'=\frac{\sigma}{V_{\rm ex}^{1/3}}K^*\boldsymbol{I}. \tag{37}$$

The data of Fig. 15(b) are recast in these terms in Fig. 15(c). It appears that the results for K^* are less scattered than for K.

To summarize, all the results obtained in Sec. IV C for monodisperse regular hexagons should be transposable to networks of fractures with any monodisperse shapes. For anisotropic polygons, K^* in Eq. (37) is a better invariant than K.

V. CONCLUDING REMARKS

A systematic study of the permeability of fracture networks has been initiated in this work. It might be more useful to emphasize here the various points that still deserve further studies.

The first one is the practical limitation of the triangulation process to a density $\rho'\sim 10$. The causes of this restriction should be found in order to increase the range of our computations to larger densities. The interest of such an extension lies mostly in the validation or lack thereof of the asymptotic regime (34).

Second, the numerical study of more complex structures should be done. The important practical case of polydisperse fractures should be addressed. Probably still more important, many field works as discussed by Sahimi [24,14] indicate that the fracture network of a rock may be fractal; this is confirmed by numerical simulations of rock fracturation; hence the investigations of the present tool should be extended as well in this direction.

Finally, the program has been devised to be able to cope with any fracture network. A direct comparison between some experimental data with a well-characterized fracture network and the output of the tool presented here would be of a very high interest.

ACKNOWLEDGMENT

Most of the computations were performed at CNUSC (subsidized by the MENESR), whose support is gratefully acknowledged.

[1] M.C. Cacas, E. Ledoux, G. de Marsily, B. Tillie, A. Barbeau, E. Durand, B. Feuga, and P. Reaudecerf, Water Resour. Res. **26**, 479 (1990).

[2] D. Billaux, J.P. Chiles, K. Hestir, and J. Long, Int. J. Rock Mech. Min. Sci. Geomech. Abstr. **26**, 281 (1989).

[3] A. Rouleau and J.E. Gale, Int. J. Rock Mech. Min. Sci. Geomech. Abstr. **24**, 99 (1987).

[4] D. Bruel and F.H. Cornet, in *Fractured and Jointed Rock Masses*, edited by L.R. Myer, N.G.W. Cook, R.E. Goodman, and C.F. Tsang (Balkema, Rotterdam, 1995).

[5] D. Billaux, *Hydrogéologie des Milieux Fracturés. Géométrie, Connectivité et Comportement Hydraulique* (Editions du BRGM, Orléans, 1990).

[6] A.W. Nordqvist, Y.W. Tsang, C.F. Tsang, B. Dverstorp, and J.

Andersson, Water Resour. Res. **28**, 1703 (1992).
[7] J. Andersson and B. Dverstorp, Water Resour. Res. **23**, 1876 (1987).
[8] B. Berkowitz and I. Balberg, Water Resour. Res. **29**, 775 (1993).
[9] K. Hestir and J.C.S. Long, J. Geophys. Res. **95**, 21 565 (1990).
[10] I. Balberg, B. Berkowitz, and G.E. Drachsler, J. Geophys. Res. **96**, B, 10 015 (1991).
[11] O. Huseby, J.-F. Thovert, and P.M. Adler, J. Phys. A **30**, 1415 (1997).
[12] P.L. George, *Génération Automatique de Maillages—Application aux Méthodes d'Éléments Finis* (Masson, Paris, 1990).
[13] I. Balberg, C.H. Anderson, S. Alexander, and N. Wagner, Phys. Rev. B **30**, 3933 (1984).
[14] M. Sahimi, *Flow and Transport in Porous Media and Fractured Rock* (VCH, Weinheim, 1995).
[15] P.M. Adler, *Porous Media* (Butterworth-Heinemann, Stoneham, MA, 1992).
[16] J.-F. Thovert, J. Sallés, and P.M. Adler, J. Microsc. **170**, 65 (1993).
[17] V.M. Mourzenko, J.-F. Thovert, and P.M. Adler, J. Phys. II **5**, 465 (1995).
[18] H. Brenner and D.A. Edwards, *Macrotransport Processes* (Butterworth-Heinemann, Stoneham, MA, 1993).
[19] D.T. Snow, Water Resour. Res. **5**, 1273 (1969).
[20] D. Stauffer and A. Aharony, *Introduction to Percolation Theory* (Taylor and Francis, London, 1994).
[21] I. Balberg, Philos. Mag. B **56**, 991 (1987).
[22] M.E. Fischer, in *Critical Phenomena*, Proceedings of the International School of Physics ''Enrico Fermi,'' Course 51, Varenna, 1971, edited by M.S. Green (Academic, New York, 1971).
[23] M.C. Cacas, Ph.D. thesis, ENSM, Paris, 1989 (unpublished).
[24] M. Sahimi, Rev. Mod. Phys. **65**, 1393 (1993).